ISSN 0031-918X, Physics of Metals and Metallography, 2023. © Pleiades Publishing, Ltd., 2023.

STRUCTURE, PHASE TRANSFORMATIONS, AND DIFFUSION

On the Morphology Variation of Graphite in Ductile Cast Iron through Severe Plastic Deformation

S. K. Kaboli-Mallak[a, b, *], N. Kheirkhahan[a, c], E. Edalati[a], Y. Kelidari[a], and A. R. Kiani-Rashid[a]

[a] *Department of Metallurgical and Materials Engineering, Faculty of Engineering, Ferdowsi University of Mashhad, Mashhad, Iran*

[b] *Key Laboratory for Advanced Materials of Ministry of Education, School of Materials Science and Engineering, Tsinghua University, Beijing, 100084 China*

[c] *Dipartimento Interateneo Di Fisica, Universita Di Bari, Bari, 70126 Italy*

**e-mail: k_kaboli_m@yahoo.com*

Received July 25, 2023; revised October 14, 2023; accepted November 5, 2023

Abstract—For decades, researchers have been concerned about the formability of manufactured wrought cast iron, with brittleness being a major issue in these alloys. To address this, the ferrite phase has been identified as a suitable matrix for cast iron deformation due to its ability to provide satisfactory ductility and avoid brittle limitations. In this study, machined parts of ductile cast iron were subjected to an annealing process at approximately 900°C for 1 h before undergoing hot plastic deformation with varying degrees of reduction. The deformation was carried out using a cylinder-covered hot compression (CCC or CCHC) technique. The primary objective of this study is to gain a microscopic understanding of hot plastically deformed ductile cast iron and propose a mathematically formulated flow strain that takes into account the contributions of the microstructure's constituent phases. This analysis aims to provide a comprehensive characterization of deformed graphite within the microstructure. Optical microscopy (OM) and scanning electron microscopy (SEM) were employed to obtain results for the characterization. The findings revealed that as the reduction increased, spheroidal graphite tended to transform into a lamellar structure, resulting in diverse properties. Additionally, a microhardness test was conducted to assess the variation in mechanical properties throughout each deformation step.

Keywords: ductile cast iron, cylinder covered hot compression, reduction, microstructure, graphite, hardness

DOI: 10.1134/S0031918X23601312

INTRODUCTION

Metal forming is an essential method employed in the manufacturing of wrought products for various industries [1–4]. Ductile Cast Iron (DCI or DI), also known as Nodular Cast Iron, Globular Graphite Iron, or Spheroidal Graphite Iron (SGI), has experienced substantial industrial production, surpassing 28 million tons worldwide in recent years. However, the COVID-19 pandemic led to a decline in global production to 23.5 million tons in 2020 [5, 6].

Forming processes play a crucial role in the fabrication of cast iron, and further investigations are needed to understand the pathways of plastic deformation. Despite its widespread use, cast iron exhibits low ductility, necessitating efforts to enhance its formability [7–10]. Rehder and Perry proposed that hot compression could be a suitable method for forming cast iron due to its inherent rigidity [11]. Hot or warm working within the austenite or multiphase stable regions has been suggested to improve the workability of cast iron [12]. Subsequent studies have focused on hot compression of the alloy at high temperatures and moderate strain rates, where recrystallization occurs simultaneously with deformation, leading to substantial work hardening [13–15]. Various severe plastic deformation techniques have been employed in both industrial and academic research [16].

The microstructural evolution of deformed spheroidal graphite cast iron has been investigated by Faisal et al., examining the parameters that influence it [17]. Shi et al. studied the anisotropy of tensile strength in ductile iron resulting from the presence of graphite [7]. Hervas and her colleagues proposed a relationship between experimentally measured nodule strain and numerical simulation at different stress-strain stages [18]. In another work, Hervas suggested a relationship for estimating void fraction based on the modified Gurson model, considering the contrasting flowability of graphite and the matrix [19]. Zhao Xin et al. attempted to describe processing maps for hot compression of ductile iron, suggesting a temperature range of 900–1000°C and a strain rate of 0.1–1 s^{-1} as suitable conditions for dynamic recrystallization [20]. This

Table 1. Chemical composition of DCI and steel cylinder

Alloy, wt %	C	Si	Mn	Ni	Al	Cr	Mo	P	S	Mg	Fe
Ductile iron	3.74	2.17	0.23	0.01	0.03	–		0.01	0.005	0.05	Bal.
Steel cylinder (CK45)	0.46	<0.40	0.65	<0.40	–	<0.40	<0.10	–	–	–	Bal.

thermo-mechanical process above the recrystallization temperature avoids work hardening, thereby increasing the material's capacity for plastic deformation.

Qi et al. proposed an engineering plastic strain rate of 0.7 within the temperature range of 700–900°C as an appropriate thermomechanical process for hot compression of ductile iron without failure [21]. Within these temperature ranges, the transformation of pearlite into austenite or ferrite, as well as grain boundary migration and dislocation movement, occur more efficiently during the compression process, resulting in a higher strain peak. Zhao et al. developed the CCC process to investigate the graphite morphology in hot-compressed ductile iron, revealing that the shape of the graphite changes from spherical to lamellar with increasing amounts of hot deformation [22]. However, further comprehensive studies are required to establish this as a well-founded research work. Another study on hot-compressed gray iron using the CCC process demonstrated that after hot deformation, graphite flakes with random orientation tended to align parallel to each other, forming a sandwich structure [23]. In this context, Wei et al. showed that the hardness and tensile strength of gray iron, when deformed using the CCC process, improved due to the extension of graphite flakes perpendicular to the compression direction and a reduction in the angle between the graphite flake tip and the compression direction. Cracks typically initiate at the graphite-matrix interface in cast iron. Therefore, reducing the measured angle leads to a reduction in stress concentration, resulting in increased tensile strength of the deformed samples [24]. Previous studies have emphasized the significant influence of graphite morphology on the material properties of cast iron [10, 25]. While there have been some research efforts focusing on the characterization of severe plastic deformation in cast iron, a more comprehensive investigation is needed to assess the microstructural changes in processed workpieces. This paper employs the CCC method (Cylinder-Covered Compression) to explore and understand the process of deforming ductile iron, aiming to provide a pathway for a thorough understanding of producing deformed cast iron components that remain free from cracks [3].

2. EXPERIMENTAL

2.1. Melting and Sample Preparation

In this research, experimental ductile iron with a specific chemical composition (as shown in Table 1) was produced using an induction furnace, following the guidelines of ASTM E351 [26]. The melt was prepared based on ASTM A536 [27] for SG40 cast iron, and FeSiMg alloy was introduced into the molten metal at a temperature of 1500°C to facilitate the formation of spherical graphite using the sandwich process. The casting process was carried out using sand molds, resulting in the production of ten bulk specimens with dimensions of 400 × 250 × 100 mm^3.

Metallic cylinders were machined from CK45 carbon steel to serve as covers for the specimens. These covers had an inner diameter of 12.5 mm, an outer diameter of 15 mm, and a height of 12 mm. The nominal composition of the steel cover casing is also provided in Table 1. To prepare the cast iron bodies for testing, cylindrical samples with a diameter of 12.5 mm and a height of 12 mm were machined from the as-cast bulk specimens.

Two sets of testing samples were prepared for the CCC (Cylinder-Covered Compression) and Non-CCC (Reference) experiments. Each set consisted of two batches, with a total of 72 testing samples per batch, ensuring sufficient samples for mechanical testing and characterization analysis.

2.2. Heat Treatment

The properties of ductile iron are influenced by factors such as composition, alloying elements, microstructure, graphite morphology, cooling rate, and heat treatment [28, 29]. To achieve a desirable microstructure with improved ductility, ferritizing annealing was performed on the covered workpieces. The annealing process was conducted in a furnace with an electrical power of 54 kW. The workpieces were heated to 900°C and held at this temperature for 1 hour. Subsequently, they were slowly cooled to 700°C at a cooling rate of 110°C/h and maintained at this temperature for 1 h. The cooling process continued by reducing the temperature to 340°C at a cooling rate of 55°C/h. Finally, the samples were cooled in air.

2.3. Thermomechanical Process

The thermomechanical process was carried out according to the parameters specified in Table 2 and illustrated in Fig. 1. After each step, the samples were heated to the optimal austenite temperature of 900°C within the suggested austenitizing range of 870–900°C [30]. They were held at this temperature for

5 minutes, followed by applying hot compression using a Gleeble 3500 machine.

To prepare the deformed work-pieces for the multi-stage CCC process, the surfaces were thoroughly cleaned to remove mill scale, oxides, loose parts, and any other discontinuities. After each pass of the thermomechanical process, the work-pieces were re-machined and re-grinded to ensure a smooth and uniform surface.

The compression process was conducted using a new cylinder as a cover casing for the cylinder-covered work-pieces. For non-covered work-pieces, they were adjusted and stacked on top of each other to maintain the role of the steel cylinder. As the process advanced, more deformed samples were added within the enclosed cylinder, as depicted schematically in Fig. 1. The deformation process continued until a 92% reduction was achieved for the covered work-pieces and a 33% reduction for the non-covered ones.

2.4. Samples Preparation

After each compression pass, specimens were prepared for characterization following the standard guidelines of ASTM E3 (Standard Guide for Preparation of Metallographic Specimens) [31]. The process involved grinding the specimens using abrasive sandpaper with varying grit sizes ranging from 80 to 1200.

Table 2. Thermomechanical process

Reduction, % 33-50-66-83-92	Compressing rate, s^{-1}: 0.01
	Temperature, °C: 900
	Cooling environment: air

Subsequently, polishing was performed using a Buehler wheel polishing machine and an oxide slurry suspension containing Al_2O_3 particles of 0.3 and 0.05 μm diameters. The mounted samples were then etched with Nital 2% solution for 2 s to enhance the microstructure visibility.

2.5. Microstructural Examination

Microstructural examination was conducted on the axially sectioned specimens, representing the compression load direction. An Optical Microscope (Olympus BX60MF5) equipped with a digital camera (JVC 10215670) and a Scanning Electron Microscope (SEM: LEO 1450VP) were utilized for microstructural analysis. Clemex Image Analyzer Software was employed for the evaluation and characterization of microstructural phases. The distribution and size of graphite were determined following the ASTM A247 (Standard Test Method for Evaluating the Microstructure of Graphite in Iron Castings) [32].

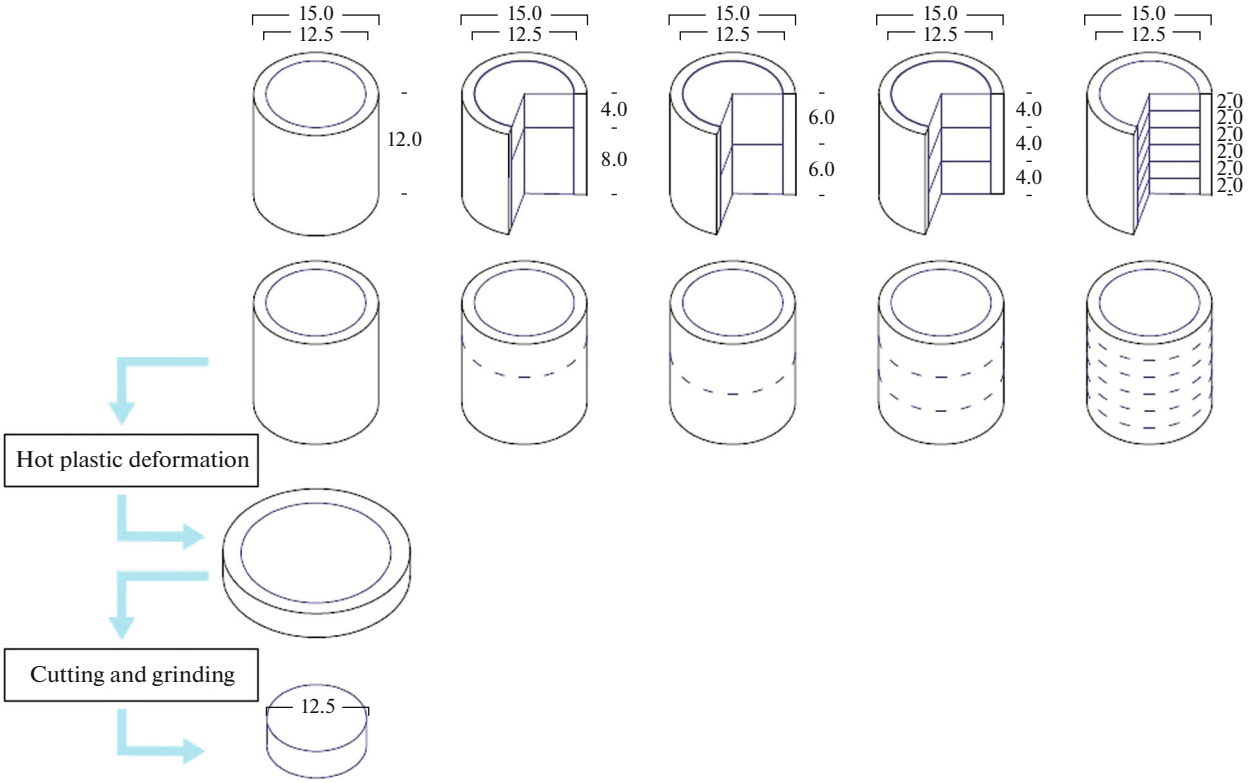

Fig. 1. Demonstration of the deformation procedure schematically.

2.6. Mechanical Testing (Hardness Test)

Mechanical testing, specifically hardness testing, was performed on the as-polished samples. Microhardness evaluation of the Ferrite phase was conducted under a load of 100 gf, while the Vickers hardness test was performed on all contributing phases using a Vickers hardness machine with a load of 150 kg. Five measurements were taken for each sample to obtain an average value. The hardness tests were carried out according to ASTM E92 (Standard Test Methods for Vickers Hardness and Knoop Hardness of Metallic Materials) [33] and ASTM E384 (Standard Test Method for Micro-indentation Hardness of Materials) [34], respectively.

3. RESULTS AND DISCUSSION

3.1. Macroscopic Evaluation

During the hot compression process, the first pass was successfully carried out on both the covered and non-covered workpieces. However, satisfactory pressing of the non-covered samples in the second pass was challenging, and it was unsuccessful in the third pass due to increasing surface irregularities. These surface irregularities hindered the attainment of a uniform final structure. The non-covered specimens lost their standard shape and exhibited crushed sections, particularly at the edges, due to slipping of the parts during the process. The inhomogeneous deformation caused by different stress concentrations resulted in an uneven depression in the samples. Previous researchers have also highlighted the importance of using cylinders as holders for hot compression of ductile iron to maintain uniform shape and integrity [35, 36]. While the steel cylinder does not directly affect the formability of cast iron due to its higher workability, its indirect positive role in maintaining the shape of ductile iron during hot compression is significant. Other researchers have also emphasized the positive role of the steel cylinder as a holder [37, 38]. Consequently, the non-covered samples were excluded from further investigation.

On the other hand, samples with cylinder covers were successfully hot-compressed up to a height reduction of 1 mm, which is a remarkable achievement in improving the formability of such a brittle material. The use of smaller sample dimensions ensured a smoother strain distribution along the testing material. Cast iron can be considered as a particulate metal matrix composite (PMMC), where graphite and the surrounding matrix exhibit different elastic and plastic behavior [39].

3.2. Microscopic Evaluation

The main focus of this study is the microstructural analysis of graphite in ductile cast iron to understand its behavior under compression loading. Certainly, the microstructural examination was performed on specimens obtained from sectioned samples oriented parallel to the direction of applied compressive stress. The microstructures of covered specimens at each compression pass are shown in Fig. 2. It can be observed that the specimens exhibit a wide distribution of spherical graphite, which is transformed into lamellar graphite as the reduction steps progress. Spheroidization (nodularity) was also detected at 87%, with an average nodule diameter of 12 μm. The nodularity measurement method will be explained in subsequent paragraphs. Figure 2a represents the microstructure of the as-cast sample, where the dominant phases are bull's eye graphite, ferrite, carbide, and ledeborite embedded in a pearlitic matrix. After annealing, many carbides were dissolved, resulting in a high ductile ferritic matrix with scattered graphite, as shown in Fig. 2b. It should be noted that iron carbide (cementite) was not observed after annealing due to dissolution, and the dominant phase of ferrite was evident.

According to the analysis using Clemex software, a decrease in grain size was observed from an average of 62 μm in the 33% hot-deformed section to 9 μm in the 92% hot-deformed section. The values mentioned in this article are the average of at least 5 different measurements for hardness test and ten separate measurements of microstructural components. This trend, along with the nucleation of ferrite grains around the graphite phase, provides strong evidence of dynamic recrystallization during the hot processes.

The results of the study indicate that the spherical graphite in ductile cast iron loses its typical shape during the hot compression process. In Fig. 2b, it can be observed that the spheroids transform into a shape resembling Cleopatra's eye (Ensi's eye) in the 33% compressed sample, and as the process progresses, they further elongate along a perpendicular direction to the compressing load.

The analysis of the graphite phase volume fraction per unit volume using Clemex software is presented in Table 3. The results demonstrate a significant increase in the volume fraction of graphite with the progression of deformation processes. This enhanced graphite volume fraction can be attributed to two factors. Firstly, secondary graphite formation occurs due to carbide dissolution, ferrite formation, and higher mass diffusion in the hot working regime, leading to carbon accumulation. Secondly, protruding graphite in compression may result from the differential flow behavior of graphite and the matrix [40, 41]. In the former case, annealing causes carbon precipitation from pearlite onto existing graphite or contributes to the formation of additional small graphite particles, while leaving behind a ferritic matrix.

The microstructural analysis of cast iron has been extensively studied over the years, with the introduc-

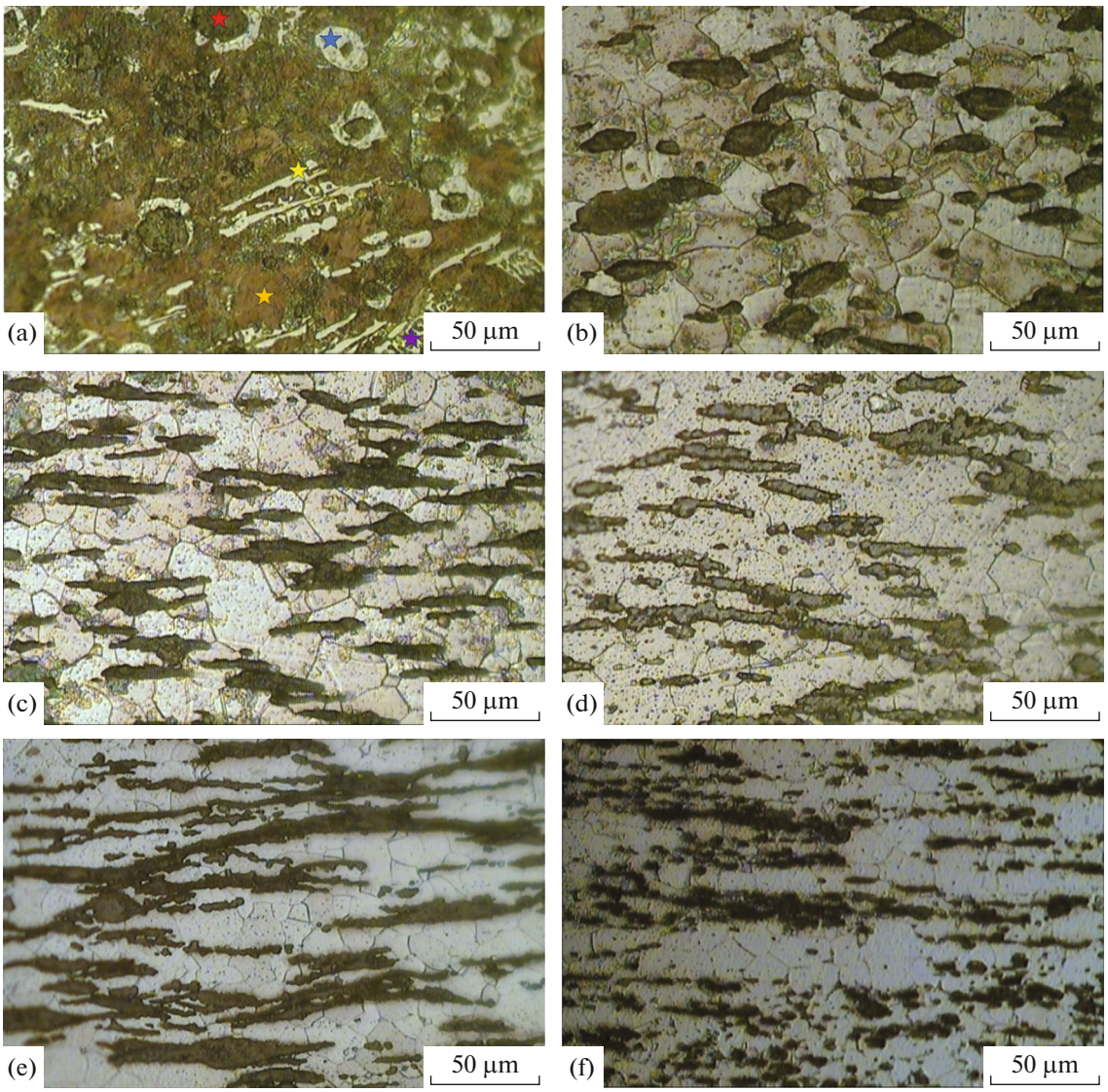

Fig. 2. Optical microscopic image of covered samples polished and etched using Nital 2% (a) as cast without deformation, (b) 33% deformation, (c) 50% deformation, (d) 66% deformation, (e) 83% deformation and (f) 92% deformation (a: red star—graphite, blue star—ferrite, yellow star—carbide, purple star—ledeburite, orange star—Pearlite; b–f: black—graphite, white—ferrite).

tion of shape factors as descriptors for graphite morphology. Different shape factors have been adopted in the characterization of graphite in cast iron samples, including aspect ratio, circularity, compactness, sphericity, or nodularity [42, 43]. The specific shape factors that receive more attention may vary depending on the type of cast iron being investigated. Further detailed definitions of these shape factors can be found in [42]. Figure 3 provides a schematic illustration of these terms along with the corresponding defining equations for deformed nodular graphite.

However, each paper's aspect ratio term has a controversial definition and needs to discriminate appropriately. So, it is worth nothing to adopt a different aspect ratio value, per the most popular references [7, 43, 44]. In this method, the aspect ratio factor should be considered $\beta = \frac{D_2}{D_1}$ where D_2 is the minor axis, and D_1 is the central axis of a particle in each level of shape from spheroid to elongated ellipsoid or flake. Using this factor and describing the requirement for an image analyzer at ASTM E2567 [45], a particle could

Table 3. Volume fraction and aspect ratio of graphite in each pass of deformation

D, %	0	33	50	66	83	92
VF_G	10.16	18.57	18.91	20.58	22.97	27.50
β_{mean}	0.923	0.468	0.113	0.091	0.063	0.040

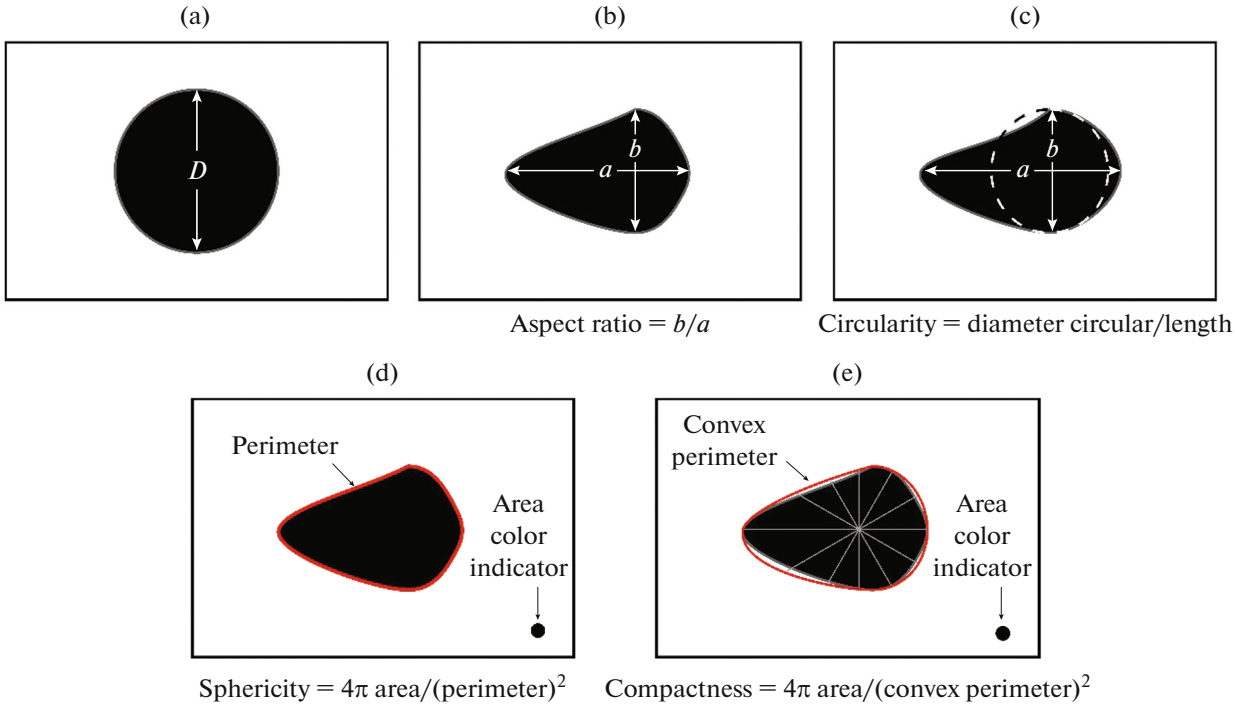

Fig. 3. Shape factors as descriptors to describe graphite morphology in a deformed spheroidal graphite, related equation and parameters. (Perimeter rubber is red). * Inscription: (b) Aspect Ratio: b/a, (c) Circularity = diameter circular/length, (d) sphericity = 4π*Area/(Perimeter)**2, (e) Compactness = 4π*Area/(Convex Perimeter)**2.

be considered a nodule if its aspect ratio is more significant than 0.5. In this contribution, the nodularity factor can be introduced as follow:

$$\text{Nodularity\%} = \frac{\text{Number of nodular graphite particles}}{\text{Number of graphite particles}}\%.$$

The nodularity factor was determined to be 87% in this study, based on the calculation involving 600 nodular graphite particles per square millimeter. It's worth noting that a non-destructive ultrasonic test has been developed to determine nodularity in cast iron, which is believed to have a significant impact on the mechanical properties of cast iron [46, 47].

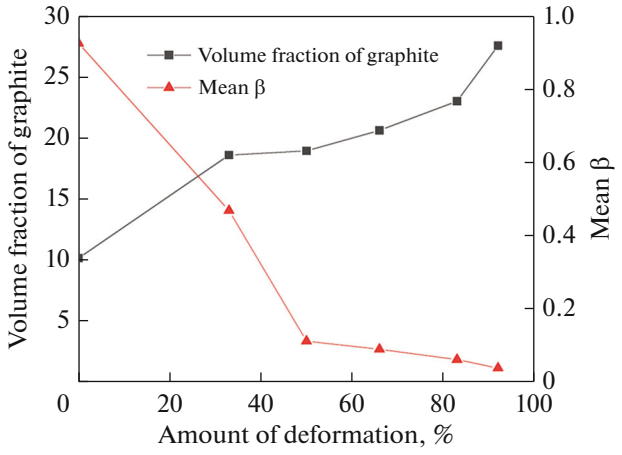

Fig. 4. Mean β (red triangle) and volume fraction of graphite (black square) in different amounts of deformation.

The aspect ratio (β) was also utilized to describe the changes in graphite shape during the deformation of ductile cast iron. The β parameter represents the success or failure in achieving the sphericity of graphite in cast iron, with a value of 1 indicating perfect spheroidal graphite. Using the Clemex software, the average β parameters were calculated and presented in Table 3 and Fig. 4. The measurement for fractured graphite considered the cumulative length of each part of the pre-united graphite.

Table 3 and Fig. 4 provide further confirmation of the formation of a lamellar structure and the collapse of nodular graphite during successive hot deformation processes. In other words, the morphology of graphite in ductile iron transformed from a spheroidal shape to a customized form resembling gray iron. This trend aligns with an approximately continuous increase in the volume fraction of graphite. At the 92% deformation stage, a significant decrease in the β factor is observed. Figure 2e illustrates that crushed graphite leads to a failure in achieving a uniform shape, resulting in the separation of graphite into distinct forms.

These findings contribute to our understanding of the microstructural changes occurring in ductile cast iron during the compression process and highlight the

influence of deformation on graphite morphology and volume fraction.

In cast iron, which can be considered a particulate metal matrix composite (PMMC), the graphite phase and the surrounding metal matrix exhibit different elastic and plastic behaviors [39]. In this issue, the overall deformation of bulk material can be estimated as:

$$\epsilon_j = \frac{h_0 - h_1}{h_0}, \tag{1}$$

where h_0 and h_1 are the bulk specimen heights before and after deformation, respectively [39]. To estimate the overall deformation of the bulk material, Eq. (1) is used. Similarly, previous researchers [44] have attempted to express the engineering strain for a graphite particle using a similar approach. However, the specific equation or expression for the engineering strain of a graphite particle is not provided in the given information.

$$e_g = \frac{h_2 - h_3}{h_2}, \tag{2}$$

where h_2 is the average diameter of graphite particle before compression test and h_3 indicates the average diameter of graphite particle after compression. The measured values were obtained from a longitudinal cross-section analysis of the direction of applied stress. The exact property for metallic matrix can be formulated for vertical cross-section measurement as follow:

$$e_m = \frac{h_4 - h_5}{h_4}, \tag{3}$$

where h_4 is the average initial metal matrix separation between two discrete graphite particles and h_5 is the same value after applying compression.

Similarly, the total (proportional) reduction of the bulk material (ϵ_t) in parallel with compressive stress may be written as:

$$\epsilon_t = \frac{(h_2 + h_4) - (h_3 + h_5)}{h_2 + h_4}. \tag{4}$$

Re-arranging:

$$\epsilon_t = \frac{(h_2 - h_3) + (h_4 - h_5)}{h_2 + h_4} = \frac{e_g}{\frac{h_2 + h_4}{h_2}} + \frac{e_m}{\frac{h_2 + h_4}{h_4}} = \frac{e_g}{1 + \frac{h_4}{h_2}} + \frac{e_m}{1 + \frac{h_2}{h_4}}. \tag{5}$$

Now, it is reasonable to define an inclusion distribution factor (F) as:

$$F = \frac{h_4}{h_2}. \tag{6}$$

Deformation ratio (K) also can be introduced as:

$$K = \frac{e_g}{e_m}. \tag{7}$$

By substituting the defined terms in (5), the re-arranged equation can be obtained as below:

$$e_t = \left(\frac{K + F}{1 + F}\right) e_m. \tag{8}$$

It is worth mentioning that a good estimation for an average value of graphite particles and their interval space can be taken from microscopic analysis of 50 different graphite and the related space.

If one calculates the aspect ratio of graphite particle, it may be capable of rewriting Eq. (2) differently as follows:

$$e_i = 1 - \beta^{2/3}, \tag{9}$$

where i is addressing term for inclusion. Thus, after simplifying, the ratio of the inclusion deformation to the metal matrix deformation is:

$$K = \frac{F\left(1 - \beta^{2/3}\right)}{e_t(1 + F) - \left(1 - \beta^{2/3}\right)}. \tag{10}$$

The information provided suggests the calculation of the deformation ratio, denoted as K, which represents the ratio of the inclusion deformation to the metal matrix deformation. This ratio depends on factors such as the size and distribution of graphite particles (represented by the shape factor in accordance to Fig. 3, which was calculated as 8.25 in this study), the total reduction (et), and the final aspect ratio of the graphite particles.

The deformation ratio, K, serves as an indicator of the relative bulk deformation, taking into account the different behaviors of graphite particles and the surrounding metallic matrix. The results presented in Fig. 5 demonstrate the calculated deformation ratios and support the findings of previous researchers, who have observed that the strain in graphite nodules is generally higher than that in the matrix. This observation holds true up to an 83% reduction in the current study, after which the integrity between the particles and matrix begins to deteriorate.

The significant increase in the deformation ratio observed at a 50% reduction is attributed to the preservation of binding between graphite nodules and the matrix, which tends to decrease as micro-voids form and coalesce. These findings contribute to the understanding of the mechanical behavior of the composite material and the deformation characteristics of the graphite inclusions.

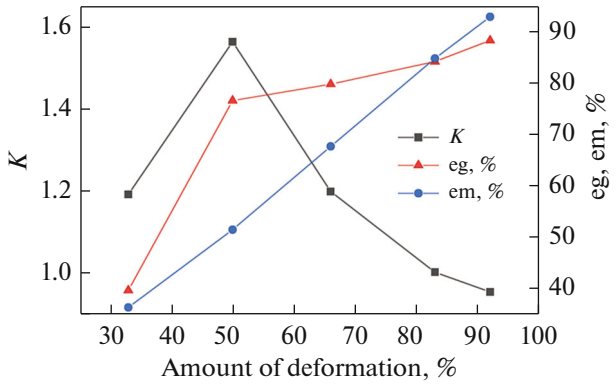

Fig. 5. The relationship between engineering strain of graphite (red triangle), engineering strain of metal matrix (blue circle) also K factor (black square) with different amounts of deformation.

Neglecting shear deformation, other researchers [18, 48] tried to calculate the true longitudinal strain of graphite particle, which is expressed as follows:

$$\varepsilon_z = \ln\frac{b}{d}. \tag{11}$$

In (11) and subsequent sections, the diameter of the pristine, unaltered graphite is denoted as "d", while the minor and major axes of the elliptically deformed graphite are respectively referred to as "a" and "b". The initial volume and final volume of graphite particles can be considered equal if there is no notable damage to graphite particles. This fact is so significant when someone wants to study the initial steps of the CCC compression test, where no graphite collapse is evident yet, and a good binding between the graphite particle and the metallic matrix remains if the initial graphite particle is considered as a spheroid and the deformed one as an ellipsoid. So, from volume constancy:

$$V_0 = V_1, \tag{12}$$

$$\frac{4}{3}\Pi\left(\frac{d}{2}\right)^3 = \frac{4}{3}\Pi\frac{b}{2}\left(\frac{a}{2}\right)^2, \tag{13}$$

having:

$$d = \sqrt[3]{a^2 b}. \tag{14}$$

Knowing the aspect ratio of graphite particle and the nature of compression, which leads to putting compress strain in height and stretching in the rest of the directions, it is applicable to relate calculated graphite true strain in three dimensions as below:

$$\varepsilon_z = \ln\frac{b}{d} = \ln\left(\frac{b}{a}\right)^{\frac{2}{3}} = \frac{2}{3}\ln\beta, \tag{15}$$

$$\varepsilon_x = \ln\frac{a}{d} = \ln\left(\frac{a}{b}\right)^{\frac{1}{3}} = -\frac{1}{3}\ln\beta. \tag{16}$$

However, one may relate true strain in X and Y directions by introducing α like:

$$\varepsilon_y = \alpha\varepsilon_x. \tag{17}$$

Assuming no change in graphite volume at the initial steps of deformation, and considering the 1–3 to address strain in x, y and z directions, one may express it as:

$$\varepsilon_1 + \varepsilon_2 + \varepsilon_3 = \varepsilon_1 + (1+\alpha)\varepsilon_3 = 0, \tag{18}$$

giving:

$$\varepsilon_3 = -\frac{1}{1+\alpha}\varepsilon_1. \tag{19}$$

As a result, total effective plastic strain as a true strain can be taken by the following formula:

$$\begin{aligned}\varepsilon\,(\text{mean}) &= \sqrt{\frac{2}{3}}(\varepsilon_1^2 + \varepsilon_2^2 + \varepsilon_3^2) \\ &= \sqrt{\frac{4\left(\alpha^2+\alpha+1\right)}{3\left(\alpha^2+2\alpha+1\right)}}\varepsilon_1 = f(\alpha)\varepsilon_1\end{aligned} \tag{20}$$

the aspect ratio of any graphite particle can be associated with the imposed equivalent plastic strain on that particle as below:

$$\begin{aligned}\ln(\beta) &= \ln\left(\frac{b}{a}\right) = \ln\left(\frac{b}{d}\right) - \ln\left(\frac{a}{d}\right) = \epsilon_1 - \epsilon_3 \\ &= \frac{2+\alpha}{1+\alpha}\epsilon_1 = \frac{2+\alpha}{f(\alpha)(1+\alpha)}\varepsilon\,(\text{mean}).\end{aligned} \tag{21}$$

Therefore, it can be seen that:

$$\varepsilon\,(\text{mean}) = \frac{f(\alpha)(1+\alpha)}{2+\alpha}\ln(\beta) = g(\alpha)\ln(\beta). \tag{22}$$

The study by Hervas et al. [18] proposed that the major axis of the ellipsoid representing the graphite particle is identical in both the X and Y directions. Another study by Bahadori-Fallah et al. [48] stated that α can be considered as 0 for plane strain mode and 1 for axisymmetric strain mode. In the current study, the axisymmetric strain mode was adopted, leading to a calculated $g(\alpha)$ value of 0.667.

However, despite the detailed approach in the previous equation, it is important to note that certain process factors can introduce errors in the estimated values during compression tests. These factors include the presence of a dead zone, friction between the testing machine and the sample, non-uniform deformation or heating processes, variations in sample volume and geometry, applied strain rate, amount of strain, and reduction.

SEM (Scanning Electron Microscopy) micrographs were obtained and presented in Fig. 6 to provide additional characterization of the graphite. These images reveal the formation of cavities on the surface of the samples when subjected to high levels of deformation. According to Eshelby's theory, the presence

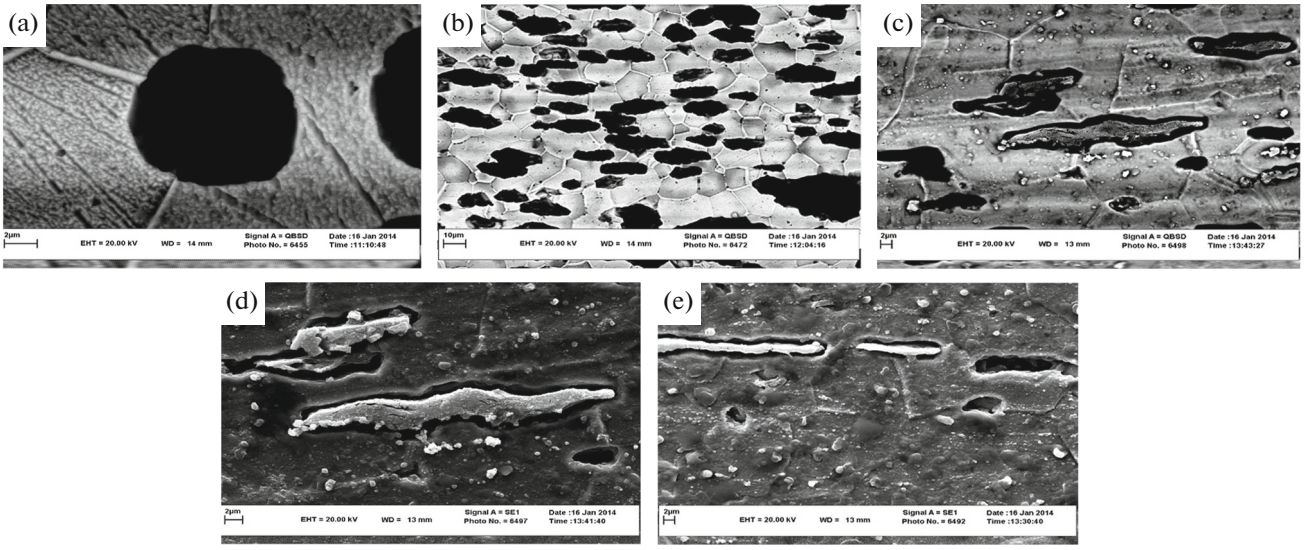

Fig. 6. (a) SEM micrographs of graphite in the cast and annealed sample, (b) the sample with 33% reduction, (c&d) the sample with 83% reduction S.E. mode & B.S. mode respectively, and (e) the sample with 92% reduction (S.E. mode).

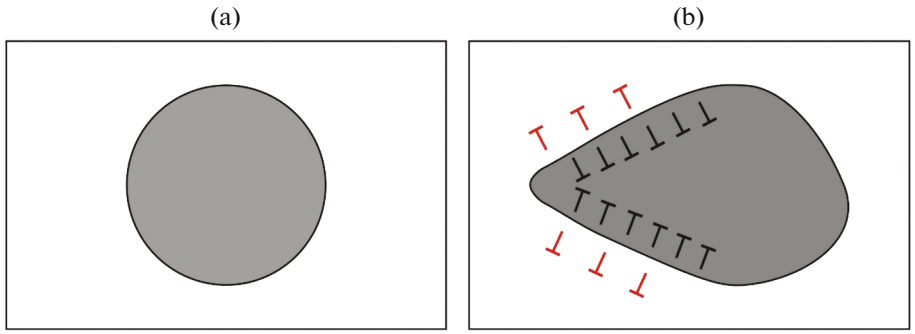

Fig. 7. Schematic of GND density at graphite-matrix interface (a) Preliminary graphite nodule, (b) Deformed graphite-nodule (Gray = graphite, black down to up indicators = GND in graphite, red up to down indicators = GND in matrix, white = matrix).

of dispersed particles and phases within the matrix can result in different ductility characteristics compared to the parent matrix. Consequently, strain incompatibility is expected to arise between these phases. To compensate for this incompatibility, geometrically necessary dislocations (GND) are generated at the graphite-matrix interface. However, in cases where the interface is weak and unable to accommodate volume changes, the strain is relieved by creating cavities. Thus, Eshelby proposed that the dislocation density and the number of cavities in multiphase materials are significantly higher compared to single-phase materials.

In accordance with Eshelby's theory, in regions experiencing high strain, the dislocation density tends to decrease due to recovery and recrystallization processes, which compete with the introduction of geometrically necessary dislocations (GNDs) [49–51]. While there have been some experimental and modeling studies attempting to explain the response of graphite to mechanical loading, there has been a lack of comprehensive research from a microstructural perspective [52–54].

The current study supports Eshelby's viewpoint, as recrystallized grains are observed in the microstructure. A schematic illustration demonstrating the formation of GND clusters, their coalescence, and the subsequent formation of voids is presented in Fig. 7. This phenomenon is an inevitable consequence of the heterogeneous response to mechanical loading between the graphite particles and the matrix. However, in the final stages of deformation, particularly at high levels of intensity.

The current study supports Eshelby's viewpoint, as recrystallized grains are observed in the microstructure. A schematic illustration demonstrating the formation of GND clusters, their coalescence, and the subsequent formation of voids is presented in Fig. 7. This phenomenon is an inevitable consequence of the

Table 4. Hardness and micro-hardness results

Reduction in cross-section (%)	0	33	50	66	83	92
Mean micro-hardness of ferrite (100 gf)	264	130	134	141	145	168
Average hardness (HV-150 kg)	282	141	147	149	156	157

heterogeneous response to mechanical loading between the graphite particles and the matrix. However, in the final stages of deformation, particularly at high levels of intensity, cavity formation becomes prominent, as depicted in Figs. 6c–6e for reductions of 83 and 92%, respectively. This suggests that the rate of defect creation (such as dislocations and vacancies) exceeds the rate of defect reduction during recovery and recrystallization processes [49–51].

Indeed, certain researchers have considered soft graphite nodules in ductile iron as voids within the material, which are susceptible to damage primarily through a micro-mechanism known as crack nucleation and continuum propagation, induced by deformation and stress concentration [35, 36, 55, 56]. In this context, void or cavity formation occurs when the motion of dislocations is not adequately accommodated at the interfaces between the graphite particles and the matrix. The stress concentration at these interfaces can lead to localized deformation and the initiation of cracks, resulting in the formation of voids within the material. The density of nucleated GNDs at the graphite-matrix interface is proportional to the strain gradient as follows [57, 58]:

$$\rho(\mathrm{GND}) \propto \alpha - d\varepsilon/dz. \quad (23)$$

The relationship between true strain (ε) and the GND density can be described by Eq. (20), where ε represents the true strain at each stage of the thermomechanical process, and z denotes the distance from the graphite-matrix interface. As the true strain increases, the GND density tends to increase as well. This phenomenon results in structural discontinuity and weakening of the bulk material, as observed in the sample with a 92% reduction in Fig. 6e. This indicates the breakdown of the graphite layers and the loss of proper connection between the matrix and the graphite. It is possible that during the production of microscopic samples, the graphite may become disengaged from the matrix. The different responses of graphite and the metal matrix to applied deformation can lead to stress concentration in certain regions, causing the flow of graphite branches and debonding at the graphite-matrix interface. Consequently, this can lead to the breakdown of the bulk cast iron structure.

3.3. Hardness Evaluation

Table 4 presents the hardness variation as a function of the hot deformation percentage.

The hardness results presented in Table 4 indicate the hardness according to Fig. 2. It is evident that the hardness of the material is greater in the pre-deformation stage of as-cast sample compared to the first pass of deformation. This can be attributed to the presence of coarse surrounding phases such as carbide or pearlite, which contribute to the higher hardness.

However, after annealing heat treatment, a softer phase like ferrite is encountered, and its micro-hardness increases with an increasing amount of compression. This increase in ferrite hardness could be attributed to factors such as incomplete recrystallization or the overcoming of introduced dislocations. Work-hardening and the disappearance of atomic arranging defects through recrystallization may also contribute to the increased hardness of the ferrite phase.

Despite the decrease in hardness caused by the formation of ferrite and the dissolution of carbides compared to the as-cast sample, there is a consistent rising trend in the hardness measurements as the deformation progresses. This suggests that other factors, such as grain refinement, strain-induced microstructural changes, are influencing the material's hardness during the thermomechanical process. Another noteworthy factor of interest pertains to carbon diffusion within atomistic defect regions, such as the Cottrell atmosphere. This phenomenon can lead to the constriction of dislocation mobility pathways, consequently bolstering the matrix's mechanical strength.

Towards the final stage of deformation, a slight change in hardness is observed due to the breakdown of the graphite phase and its further lateral distribution. The non-covered sample in the as-cast condition exhibited a micro-hardness of 258 Vickers for ferrite and an overall hardness of 280 Vickers. After 33% compression, the non-covered sample showed a micro-hardness of 132 Vickers for ferrite and an overall hardness of 143 Vickers.

4. CONCLUSIONS

In conclusion, this research successfully applied a thermomechanical process to ductile cast iron (DCI or DI) using the Cylinder Covered hot Compression (CCC) method at 900°C and 0.01S-1, followed by cooling in ambient air. The following key findings were obtained:

(1) The thermomechanical process led to an increase in the volume fraction of the graphite phase, despite a decrease in its mean aspect ratio. This resulted in a morphological change of graphite from spheroidal to lamellar.

(2) Through hot plastic deformation of the as-cast samples, a significant decrease in the grain size of the

ductile cast iron was observed. The grain size reduced from 62 μm in the 33% deformed section to 9 μm in the 92% deformed section.

(3) The use of a Cylinder in the hot forming technique was found to play an indirect role in maintaining the bulk integrity of the material. However, it was observed that reductions greater than 66% are not recommended as ductile cast iron tends to lose structural integrity between the matrix and graphite phases. This was confirmed through SEM micrographs, where the 92% reduction resulted in shattered graphite and a weak structure.

(4) The strain and shape factor equations indicated that graphite nodules experienced higher strain compared to the metallic matrix, especially in the initial stages of deformation. This disparity should be taken into account during the design of deformation processes.

(5) A consistent increasing trend in hardness was observed as the deformation progressed. This may be attributed to factors such as incomplete recrystallization, the introduction of dislocation colonies, and work-hardening. However, in the final stages, the hardness showed a slight change due to the breakdown and disassembly of graphite particles.

Overall, this study provides valuable insights into the thermomechanical processing of ductile cast iron, including the evolution of graphite morphology, grain refinement, structural integrity considerations, and hardness changes. These findings contribute to a better understanding of the material's behavior and can inform future optimization of thermomechanical processes for ductile cast iron applications.

ACKNOWLEDGMENTS

The authors would like to thank the Faculty of Engineering of Ferdowsi University in Mashhad for supporting the implementation of this study. The first author is also incredibly grateful to Prof. Hao Chen for his friendly helping attitude and comments. The first author also thanks Radfarman Company and its staff (Mr. Masoumi, Mr. Tabesh, and Mr. Ramesh) for supporting laboratory services.

FUNDING

This work was supported by ongoing university funding. No additional grants to carry out or direct this particular research were obtained.

CONFLICT OF INTEREST

The authors of this work declare that they have no conflicts of interest.

REFERENCES

1. J. G. Lenard and M. E. Davies, "An experimental study of heat transfer in metal-forming processes," CIRP Ann. **41**, 307–310 (1992). https://doi.org/10.1016/s0007-8506(07)61210-4
2. Y. Estrin and A. Vinogradov, "Extreme grain refinement by severe plastic deformation: A wealth of challenging science," Acta Mater. **61**, 782–817 (2013). https://doi.org/10.1016/j.actamat.2012.10.038
3. S. V. Divinski, K. A. Padmanabhan, and G. Wilde, "Microstructure evolution during severe plastic deformation," Philos. Mag. **91**, 4574–4593 (2011). https://doi.org/10.1080/14786435.2011.615349
4. A. Azushima, R. Kopp, A. Korhonen, D. Y. Yang, F. Micari, G. D. Lahoti, P. Groche, J. Yanagimoto, N. Tsuji, A. Rosochowski, and A. Yanagida, "Severe plastic deformation (SPD) processes for metals," CIRP Ann. **57**, 716–735 (2008). https://doi.org/10.1016/j.cirp.2008.09.005
5. "Census of World Casting Production: Global Casting Production Growth Stalls," Mod. Casting Mag. **109**, 24–25 (2019).
6. "Census of World Casting Production: Global Casting Production Growth Stalls," Mod. Casting Mag. **109**, 26–27 (2019).
7. J. Shi, S. Zou, and R. W. Smith, "Effect of elongated graphite on mechanical properties of hot-rolled ductile iron," JMEP **3**, 657–663 (1994). https://doi.org/10.4236/msa.2019.106032
8. Z. R. He, G. X. Lin, and S. Ji, "Deformation and fracture of cast iron with an optimized microstructure," Mater. Charact. **38**, 251–258 (1997). https://doi.org/10.1016/s1044-5803(97)00080-6
9. T. El-Bitar and E. El-Banna, "Contribution of forming parameters on the properties of hot rolled ductile cast iron alloys," Mater. Lett. **31**, 145–150 (1997). https://doi.org/10.1016/s0167-577x(96)00254-6
10. V. Di Cocco, F. Lacoviello, and M. Cavallini, "Damaging micromechanisms characterization of a ferritic ductile cast iron," Eng. Fract. Mech. **77**, 2016–2023 (2010). https://doi.org/10.1016/j.engfracmech.2010.03.037
11. J. A. Rehder, "Specification for wrought iron rolled or forged blooms and forgings," Iron Age **168**, 229–233 (1951). https://doi.org/10.1520/a0073-66
12. M. Soliman, A. Nofal, and H. Palkowski, "Alloy and process design of thermo-mechanically processed multiphase ductile iron," Mater. Des. **87**, 450–465 (2015). https://doi.org/10.1016/j.matdes.2015.07.159
13. T. Sakai, A. Belyakov, R. Kaibyshev, H. Miura, and J. J. Jonas, "Dynamic and post-dynamic recrystallization under hot, cold and severe plastic deformation conditions," Prog. Mater. Sci. **60**, 130–207 (2014). https://doi.org/10.1016/j.pmatsci.2013.09.002
14. H. J. Mcqueen, "Development of dynamic recrystallization theory," Mater. Sci. Eng., A **387-389**, 203–208 (2014). https://doi.org/10.1016/j.msea.2004.01.064
15. K. C. Le and D. M. Kochmann, "A simple model for dynamic recrystallization during severe plastic defor-

mation," Arch. Appl. Mech. **79**, 579–586 (2009). https://doi.org/10.1007/s00419-008-0280-z

16. E. Bagherpour, N. Pardis, M. Reihanian, and R. Ebrahimi, "An overview on severe plastic deformation: Research status, techniques classification, microstructure evolution, and applications," Int. J. Adv. Manuf. Technol. **100**, 1647–1694 (2019). https://doi.org/10.1007/s00170-018-2652-z
17. M. Faisal, E. El-Shenawy, and M. A. Taha, "Effect of deformation parameters on microstructural evolution of GGG 40 spheroidal graphite cast iron alloy," Mater. Sci. Appl. **10**, 433–450 (2019). https://doi.org/10.4236/msa.2019.106032
18. I. Hervas, M. B. Bettaieb, A. Thuault, and E. Hug, "Graphite nodule morphology as an indicator of the local complex strain state in ductile cast iron," Mater. Des. **52**, 524–532 (2013). https://doi.org/10.1016/j.matdes.2013.05.078
19. I. Hervas, A. Thuault, and E. Hug, "Damage analysis of a ferritic SiMo ductile cast iron submitted to tension and compression loadings in temperature," Metals **5**, 2351–2369 (2019). https://doi.org/10.3390/met5042351
20. X. Zhao, X. Yang, and T. Jing, "Processing maps for use in hot working of ductile iron," J. Iron Steel Res. Int. **18** (4), 48–51 (2011). https://doi.org/10.1016/s1006-706x(11)60049-6
21. K. Qi, F. Yu, F. Bai, Z. Yan, Z. Wang, and T. Li, "Research on the hot deformation behavior and graphite morphology of spheroidal graphite cast iron at high strain rate," Mater. Des. **30**, 4511–4515 (2009). https://doi.org/10.1016/j.matdes.2009.05.019
22. X. Zhao, T. F. Jing, Y. W. Gao, J. F. Zhou, and W. Wang, "A new SPD process for spheroidal cast iron," Mater. Lett. **58**, 2335–2339 (2004). https://doi.org/10.1016/j.matlet.2004.01.034
23. X. Zhao, J. Wang, and T. Jing, "Gray cast iron with directional graphite flakes produced by cylinder covered compression process," J. Iron Steel Res. Int. **14** (5), 52–55 (2007). https://doi.org/10.1016/s1006-706x(07)60074-0
24. W. Wei, T. Jing, Y. Gao, G. Qiao, and X. Zhao, "Properties of a gray cast iron with oriented graphite flakes," J. Mater. Process. Technol. **182**, 593–597 (2007). https://doi.org/10.1016/j.jmatprotec.2006.09.028
25. A. Ghahremaninezhad and K. Ravi-Chandar, "Deformation and failure in nodular cast iron," Acta Mater. **60**, 2359–2368 (2012). https://doi.org/10.1016/j.actamat.2011.12.037
26. *ASTM E351, Standard Test Methods for Chemical Analysis of Cast Iron-All Types*. https://doi.org/10.1520/e0351-18
27. *ASTM A536, Standard Specification for Ductile Iron Castings*. https://doi.org/10.1520/a0536-84r19e01
28. N. Haghdadi, B. Bazaz, H. R. Erfanian-Naziftoosi, and A. R. Kiani-Rashid, "Microstructural and mechanical characteristics of Al-alloyed ductile iron upon casting and annealing," Int. J. Miner., Metall., Mater. **19**, 812–820 (2012). https://doi.org/10.1007/s12613-012-0633-z
29. A. Shayesteh-Zeraati, H. Naser-Zoshki, and A. R. Kiani-Rashid, "Microstructural and mechanical properties (hardness) investigations of Al-alloyed ductile cast iron," J. Alloys Compd. **500**, 129–133 (2010). https://doi.org/10.1016/j.jallcom.2010.04.003
30. J. L. Dossett and C. V. White, "Introduction to cast iron heat treatment," in *Heat Treating of Irons and Steels*, Ed. by J. L. Dossett and G. E. Totten, ASM Handbook, Vol. 4D (ASM International, 2014), pp. 483–492. https://doi.org/10.31399/asm.hb.v04d.a0005945
31. *ASTM E3, Standard Guide for Preparation of Metallographic Specimens*. https://doi.org/10.1520/e0003-11r17
32. *ASTM A247, Standard Test Method for Evaluating the Microstructure of Graphite in Iron Castings*. https://doi.org/10.1520/a0247-19
33. *ASTM E92, Standard Test Methods for Vickers Hardness and Knoop Hardness of Metallic Materials*. https://doi.org/10.1520/e0092-16
34. *ASTM E384, Standard Test Method for Microindentation Hardness of Materials*. https://doi.org/10.1520/e0384-99
35. A. S. Chaus, J. Sojka, and A. I. Pokrovskii, "Effect of hot plastic deformation on microstructural changes in cast iron with globular graphite," Phys. Met. Metallogr. **114**, 85–94 (2013). https://doi.org/10.1134/s0031918x13010031
36. N. Bonora and A. Ruggiero, "Micromechanical modeling of ductile cast iron incorporating damage. Part I: Ferritic ductile cast iron," Int. J. Solids Struct. **42**, 1401–1424 (2005). https://doi.org/10.1016/j.ijsolstr.2004.07.025
37. X. Zhao and T.-F. Jing, "Effect of sandwich structure on mechanical properties of gray cast iron plates," in *Advanced Design and Manufacture to Gain a Competitive Edge*, Ed. by X. T. Yan, C. Jiang, and B. Eynard (Springer, London, 2008), pp. 241–247. https://doi.org/10.1007/978-1-84800-241-8_26
38. J. Bača and A. S. Chaus, "Effect of plastic deformation on the structure and properties of cast iron with globular graphite," Met. Sci. Heat Treat. **46**, 188–191 (2004). https://doi.org/10.1023/b:msat.0000043098.43295.94
39. S. Balos and L. Sidjanin, "Microdeformation of soft particles in metal matrix composites," J. Mater. Process. Technol. **209**, 482–487 (2009). https://doi.org/10.1016/j.jmatprotec.2008.02.015
40. P. Rubin, R. Larker, E. Navara, and M. Antti, "Graphite formation and dissolution in ductile irons and steels having high silicon contents: Solid-state transformations," Metallogr., Microstructure, Anal. **7**, 587–595 (2018). https://doi.org/10.1007/s13632-018-0478-6
41. D. R. Askeland and N. Birer, "Secondary graphite formation in tempered nodular cast iron weldments," Weld. J. **58**, 337–341 (1979).
42. R. Ruxanda and D. M. Stefanescu, "Graphite shape characterisation in cast iron—From visual estimation to fractal dimension," Int. J. Cast Met. Res. **14**, 207–216 (2002). https://doi.org/10.1080/13640461.2002.11819439

43. J. Shi, M. Ghoreshy, R. W. Smith, and J. J. M. Too, "The use of spheroidal graphite cast irons to develop forgeability criteria based on local strain measurements," J. Eng. Mater. Technol. **111**, 26–31 (1989). https://doi.org/10.1115/1.3226429

44. J. Shi, M. A. Savas, B. J. Yang, and R. W. Smith, "Spheroidal graphite ferritic cast iron—An ideal model material to examine the deformation a single phase matrix containing soft-spheroidal inclusions," Int. J. Cast Met. Res. **16**, 215–220 (2003). https://doi.org/10.1080/13640461.2003.11819585

45. *ASTM E2567, Standard Test Method for Determining Nodularity and Nodule Count in Ductile Iron Using Image Analysis*. https://doi.org/10.1520/e2567-16a

46. Z. Wang, X. Zhang, F. Xu, K. Qian, and K. Chen, "Effect of nodularity on mechanical properties and fracture of ferritic spheroidal graphite iron," China Foundry **16**, 386–392 (2019). https://doi.org/10.1007/s41230-019-9080-z

47. D. Agnoletto, G. V. B. Lemos, A. B. Beskow, C. R. D. L. Lessa, and A. Reguly, "Methodology for determination of degree of nodularity in a ductile cast iron GGG 40 by ultrasonic velocity test," South. Braz. J. Chem. **26** (26), 10–16 (2018). https://doi.org/10.48141/sbjchem.v26.n26.2018.15_2018.pdf

48. J. Bahadori-Fallah, M. H. Farshidi, and A. R. Kiani-Rashid, "Equal channel angular pressing of spheroidal graphite cast iron," Mater. Res. Express **6**, 066542 (2019). https://doi.org/10.1088/2053-1591/ab0dcf

49. J. D. Eshelby, "The determination of the elastic field of an ellipsoidal inclusion, and related problems," Proc. R. Soc. London, Ser. A: Math. Phys. Sci. **241** (1226), 376–396 (1957). https://doi.org/10.1098/rspa.1957.0133

50. J. D. Eshelby, "The elastic field outside an ellipsoidal inclusion," Proc. R. Soc. London. Ser. A. Math. Phys. Sci. **252** (1271), 561–569 (1959). https://doi.org/10.1098/rspa.1959.0173

51. J. D. Eshelby, "Elastic inclusions and inhomogeneities," Prog. Solid Mech. **2**, 89–140 (1961).

52. M. Lukhi, M. Kuna, and G. Hütter, "Micromechanical simulation of fatigue in nodular cast iron under stress-controlled loading," Mater. Des. Process. Commun. **3**, e214 (2020). https://doi.org/10.1002/mdp2.214

53. Y. B. Zhang, T. Andriollo, S. Fæster, R. Barabash, R. Xu, N. Tiedje, J. Thorborg, J. Hattel, D. Juul Jensen, and N. Hansen, "Microstructure and residual elastic strain at graphite nodules in ductile cast iron analyzed by synchrotron X-ray microdiffraction," Acta Mater. **167**, 221–230 (2019). https://doi.org/10.1016/j.actamat.2019.01.038

54. M. Mendas, S. Benayoun, M. H. Miloud, and I. Zidane, "Microhardness model based on geometrically necessary dislocations for heterogeneous material," J. Mater. Res. Technol. **15**, 2792–2801 (2021). https://doi.org/10.1016/j.jmrt.2021.09.093

55. T. Andriollo, K. Hellström, M. R. Sonne, J. Thorborg, N. Tiedje, and J. Hattel, "Uncovering the local inelastic interactions during manufacture of ductile cast iron: How the substructure of the graphite particles can induce residual stress concentrations in the matrix," J. Mech. Phys. Solids **111**, 333–357 (2018). https://doi.org/10.1016/j.jmps.2017.11.005

56. T. Andriollo, S. Fæster, and G. Winther, "Probing the structure and mechanical properties of the graphite nodules in ductile cast irons via nano-indentation," Mech. Mater. **122**, 85–95 (2018). https://doi.org/10.1016/j.mechmat.2018.03.010

57. H. Gao, Y. Hang, W. D. Nix, and J. W. Hutchinson, "Mechanism-based strain gradient plasticity? I. Theory," J. Mech. Phys. Solids **47**, 1239–1263 (1999). https://doi.org/10.1016/s0022-5096(98)00103-3

58. Y. B. Zhang, T. Andriollo, S. Fæster, R. Barabash, R. Xu, N. Tiedje, J. Thorborg, J. Hattel, D. Juul Jensen, and N. Hansen, "Microstructure and residual elastic strain at graphite nodules in ductile cast iron analyzed by synchrotron X-ray microdiffraction," Acta Mater. **167**, 221–230 (2019). https://doi.org/10.1016/j.actamat.2019.01.038

59. N. A. Fleck, M. F. Ashby, and J. W. Hutchinson, "The role of geometrically necessary dislocations in giving material strengthening," Scr. Mater. **48**, 179–183 (2003). https://doi.org/10.1016/s1359-6462(02)00338-x